Pergamon

J. Aerosol Sci. Vol. 29, No. 7, pp. 839–853, 1998

Printed in Great Britain
0021-8502/98 \$19.00 + 0.00

PII: S0021-8502(97)00433-3

PERFORMANCE EVALUATION OF AN API AEROSIZER™

Chuen Jinn Tsai,*[†] Hung Min Chein,[‡] Shu Ting Chang* and Jong Yoh Kuo[§]

* Institute of Environmental Engineering, National Chiao Tung University, No. 75 Poai St., Hsin Chu, Taiwan
[‡] Center for Industrial Safety and Health Technology, Industrial Technology Research Institute,
Hsin Chu, Taiwan
[§] Institute of Aeronautics and Astronautics, National Cheng Kung University, Tainan, Taiwan

(*First received* 4 *April* 1997; *and in final form* 10 *July* 1997)

Abstract—A numerical method was developed to simulate the compressible flow field and particle trajectory in an API Aerosizer™. Experimental particle time-of-flights (τ_{TOF}) data using monodisperse solid and liquid particles were also obtained. Theoretical particle τ_{TOF} results were compared with the present experimental data and those of Cheng *et al.* (1993, *J. Aerosol Sci.* **26,** 501–514). Good agreement was found for solid particles. The original τ_{TOF} calibration for the API Aerosizer™ was found to underestimate measured τ_{TOF} mainly because of the assumption of one-dimensional flow in the nozzle, and incorrect use of the particle drag coefficient in the supersonic flow field. Effects of decreasing ambient pressure and increasing particle density on increasing τ_{TOF} were found to be important. © 1998 Elsevier Science Ltd. All rights reserved

INTRODUCTION

The TSI Aerodynamic Particle Sizer™ (APS 33B, TSI Incorp., St Paul, MN, U.S.A.) and API Aerodynamic Aerosizer™ (Amherst Process Instruments Incorp., Amherst, MA, U.S.A) are the two most widely used time-of-flight aerosol spectrometers which measure particle aerodynamic diameter (d_{ae}) of the airborne particles. These two instruments differ in the operating flow regime and the applicable range of particle sizes. The TSI APS™ operates essentially in the subsonic flow regime, while the API Aerosizer™ operates under the choked flow condition at the nozzle and the air flow becomes supersonic as it continues to expand in the downstream low-pressure chamber. The aerodynamic size range of the TSI APS™ is from 0.48 to 30 μm while the API Aerosizer™ claims to measure the particle sizes from 0.5 to 200 μm, if the nozzle diameter is 750 μm. Recently, a review of the working principle, previous studies and current problems of these two instruments has been published by Baron *et al.* (1993).

Extensive experimental and theoretical results have been documented in the open literature for the TSI APS™. Several previous researchers have discussed calibration and non-Stokesian correction of the instrument (Chen *et al.*, 1985; Baron, 1986; Wang and John, 1987, 1989; Ananth and Wilson, 1988; Chen *et al.*, 1990; Cheng *et al.*, 1990; Lee *et al.*, 1990; Rader *et al.*, 1990; Brockmann and Rader, 1990; Heitbrink *et al.*, 1991; Marshall *et al.*, 1991). Particle density, dynamic shape factor, particle coincidence, gas viscosity, gas density and ambient conditions have been shown to be the main factors that influence the accuracy of the measured aerodynamic diameter. Effects of these factors can be properly corrected based on the theoretical and experimental study of the particle τ_{TOF} response of the instrument. Other researchers have discussed the effect of liquid droplet deformation on sizing accuracy (Griffiths *et al.*, 1986; Baron, 1986; Chen *et al.*, 1990). High acceleration in the APS™ nozzle distorts the spherical droplets into an oblate spheroidal shape with the maximum cross section perpendicular to the direction of motion. As a result, the liquid droplets experience higher acceleration and appear smaller than the expected aerodynamic diameter.

[†] Author to whom correspondence should be addressed.

In addition to the problems related to sizing accuracy, large particles were found to be depleted from the sampled aerosol by super-isokinetic sampling at the entrance of the inlet, and inertial impaction on the inner nozzle of the TSI APS™ (Kinney and Pui, 1995). These problems are expected to exist in the API Aerosizer™ too.

In contrast, studies of the performance of the API Aerosizer™ have rarely been published in the literature. The design of this instrument is based on the aerosol beam research of Dahneke (1973), Dahneke and Padliya (1977), Cheng and Dahneke (1979), and Dahneke and Cheng (1979). To describe the compressible flow near the centerline of a nozzle–jet system, Dahneke and Cheng (1979) assumed frictionless, isentropic flow in the converging nozzle, and a fitting formula, originally developed by Ashkenas and Sherman (1966), for the transonic and supersonic flow at the axis of the free jet. Based on the flow field, simulated results of narrow angle aerosol beam diameter were shown to agree well with the experimental data. For the API Aerosizer™, the original calibration curve of particle τ_{TOF} versus particle diameter was calculated based on the flow field obtained from the above method. Particle trajectory and particle τ_{TOF} were then calculated from the particle equation of motion involving the use of the ultra-Stokesian drag coefficient C_{d} defined as follows (Dahneke and Cheng, 1979):

$$C_{\mathrm{d}} = \frac{24}{\mathrm{Re_p}}(1 + 0.106\mathrm{Re_p^{0.856}}). \tag{1a}$$

The second term in the above equation is a correction factor for the Stokes law when the particle Reynolds number, $\mathrm{Re_p}$, is greater than 0.1. $\mathrm{Re_p}$ is calculated based on the relative velocity of the particle with respect to the gas flow. The above equation is applicable only when $\mathrm{Re_p}$ is less than 50 and the flow is incompressible. Another expression for C_{d}, proposed by Rader and Marple (1985), is

$$C_d = \frac{24}{\mathrm{Re_p}}(1 + 0.0916\mathrm{Re_p}), \quad \mathrm{Re_p} < 5 \tag{1b}$$

$$C_{\mathrm{d}} = \frac{24}{\mathrm{Re_p}}(1 + 0.158\mathrm{Re_p^{2/3}}), \quad 5 < \mathrm{Re_p} < 1000. \tag{1c}$$

Cheng *et al.* (1993) have evaluated the performance of two API Aerosizer™s by using spherical uniform-sized polystyrene latex (PSL), glass bead particles (d_{ae}, 1–150 μm), as well as non-spherical natrojarosite particles (d_{ae}, 4–18 μm). It was found that the Aerosizer™ overestimated the particle sizes by as much as 25% at an reduced ambient pressure of 625 mmHg. On the other hand, the Aerosizer™ underestimated the sizes of non-spherical natrojarosite particles by as much as 50%.

In order to better understand the performance of the API Aerosizer™, we have developed a numerical method to simulate the two-dimensional compressible flow field in the nozzle and free jet regions of the API Aerosizer™. Particle trajectory and τ_{TOF} between the two laser beams have been calculated based on the simulated flow field and particle equation of motion using a proper expression for the particle drag coefficient in the compressible flow regime. In the experiment, monodisperse PSL and ammonium fluorescein particles as well as liquid oleic acid particles were generated and introduced into the Aerosizer™ to obtain the experimental data on τ_{TOF} for different particle diameters. The experimental data thus obtained as well as those of Cheng *et al.* (1993) are compared with calculated results. Effects of ambient conditions on τ_{TOF} are also investigated numerically.

NUMERICAL

Governing equations for flow field

It is assumed that the air flow in the Aerosizer™ is inviscid and compressible. Two-dimensional Euler equations for the axisymmetric coordinate system can be written in non-dimensional form as

$$\frac{\partial U}{\partial t} + \frac{\partial E}{\partial z} + \frac{\partial G}{\partial r} + H = 0, \tag{2}$$

where

$$U = \begin{bmatrix} \rho \\ \rho u \\ \rho v \\ e \end{bmatrix}, \quad E = \begin{bmatrix} \rho u \\ \rho u^2 + P \\ \rho uv \\ (e+P)u \end{bmatrix}, \quad G = \begin{bmatrix} \rho v \\ \rho uv \\ \rho v^2 + P \\ (e+P)v \end{bmatrix}, \quad H = \frac{1}{r}\begin{bmatrix} \rho v \\ \rho uv \\ \rho v^2 \\ (e+P)v \end{bmatrix} \tag{3}$$

The unknown variables ρ, u, v and e represent the gas density, velocity components in z (axial) and r (radial) directions and total energy per unit volume, respectively. The working fluid (air) is assumed to be perfect, and the pressure P is defined by

$$P = (\gamma - 1)\left[e - \frac{\rho}{2}\left(u^2 + v^2\right)\right], \tag{4}$$

where the ratio of specific heat γ, is typically taken as 1.4.

Numerical algorithm for flow field

By integrating equation (2) over space and applying Gaussian theorem, the following integral form is obtained:

$$\frac{\partial}{\partial t}\iint_{\Omega} U \,\mathrm{d}A + \int_{\partial\Omega} (E\mathbf{i} + G\mathbf{j})\cdot\mathbf{n}\,\mathrm{d}l + \iint_{\Omega} H\,\mathrm{d}A = 0, \tag{5}$$

where $\mathbf{n}$ is the outward unit normal vector. The variable Ω is the domain of computation, and $\partial\Omega$ is the boundary of the corresponding domain. The cell-vertex scheme is used in this study wherein the flow variables, such as V_i and V_j shown in Fig. 1, are stored at the vertices of a polygonal element. By connecting the centroid of each element to the midpoints of its sides, the elements are broken into sub-elements and a dual mesh is formed. As shown in Fig. 1, a dual mesh cell, C_i, is defined by the collection of sub-elements that share the same vertex V_i, and the boundary of the cell is denoted by ∂C_i. Assuming that the flow variables at the vertex V_i have an average value of the integrated variables in C_i, equation (5) can be written as

$$\mathrm{AREA}(C_i)\left(\frac{\partial U}{\partial t} + H\right) = -\int_{\partial C_i} F(\mathbf{n})\,\mathrm{d}l, \tag{6}$$

where AREA(C_i) is the area of the cell C_i, and $F(\mathbf{n})$ is the flux oriented along the outward unit normal $\mathbf{n}$ (i.e. $F(\mathbf{n}) = (n_z E + n_r G)$). To achieve time integration of the left-hand side of equation (6), a fourth-order Runge–Kutta scheme with non-standard weighting, local time

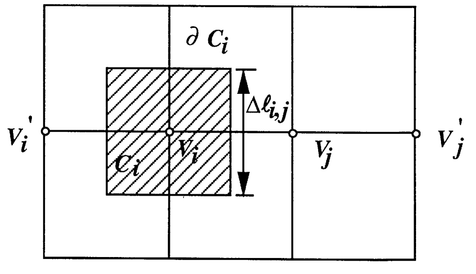

Fig. 1. A schematic diagram of the polygonal elements and dual cell. (C_i, dual cell; V_i and V_j, vertices; V_i' and V_j', ghost nodes).

steps and residual smoothing have been introduced (Whitaker *et al.*, 1980). In the current cell-vertex formulation, the right-hand side of equation (6) is evaluated as

$$\int_{\partial C_i} F(\mathbf{n})\,\mathrm{d}l = \sum_{j\,=\,L(V_i)} F_{i,j}\Delta l_{i,j}, \tag{7}$$

where $L(V_i)$ is the list of vertices surrounding V_i and the subscript j denotes the vertices contained in $L(V_i)$. $F_{i,j}$ represents the numerical approximation for the oriented flux across the dual cell edge with the boundary length $\Delta l_{i,j}$ (see Fig. 1).

In order to implement the upwind approach, Roe's (1981) flux difference splitting is employed. The flux at the cell interface, $F_{i,j}$ can be expressed as a function of two fluid dynamic states (U^{L} and U^{R}) as

$$F_{i,j} = H(U^{\mathrm{L}}, U^{\mathrm{R}}) = \tfrac{1}{2}(F_{\mathrm{L}} + F_{\mathrm{R}} - |A|(U^{\mathrm{R}} - U^{\mathrm{L}})), \tag{8}$$

where $|A|$ is a positive-definite matrix formed from the flux Jacobian $\partial F/\partial U$ (Roe, 1981) and the superscripts R and L indicate the right and left fluid states, respectively. To achieve a higher-order upwind scheme, the left and right Riemann states U^{L} and U^{R} are obtained by following a preprocessing approach. In the present work, MUSCL differencing (Anderson *et al.*, 1986) is utilized to interpolate the properties at the cell interface using the variables stored at the cell vertices. In the interpolation procedure, both central and upstream differences are required. The ghost nodes, V_i' and V_j' (see Fig. 1), which are located equidistantly along the line connecting are introduced.

To prevent numerical oscillations near the high gradient regions, the minimum-modulus (MINMOD) limiter function (Anderson *et al.*, 1986) is employed. By combining the characteristic variables with the limiter function, the MUSCL differencing formulae can be written as

$$U^{\mathrm{L}} = U_i + \tfrac{1}{4}\{(1-k)\bar{\Delta}_- + (1+k)\bar{\Delta}_+\}\,U_i, \tag{9a}$$

$$U^{\mathrm{R}} = U_i - \tfrac{1}{4}\{(1-k)\bar{\Delta}_+ + (1+k)\bar{\Delta}_-\}\,U_i, \tag{9b}$$

The definitions of $\bar{\Delta}_-$ and $\bar{\Delta}_+$ are given as

$$\bar{\Delta}_- U = \min\operatorname{mod}(\Delta_- U, \beta\Delta_+ U), \tag{10a}$$

$$\bar{\Delta}_+ U = \min\operatorname{mod}(\Delta_+ U, \beta\Delta_- U), \tag{10b}$$

$\Delta_-(U_i) = U_i - U_i'$, $\Delta_+(U_i) = U_i'' - U_i$, $\Delta_-(U_j) = U_j - U_j'$, and $\Delta_+(U_j) = U_j' - U_j$. The parameter κ, which controls the spatial accuracy, is taken to be 1/3, and the compression factor β not greater than $(3-\kappa)/(1-\kappa)$.

Boundary conditions for flow field

The flow tangency at the wall is specified and the pressure is estimated by using z- and r-momentum equations as follows:

$$\rho(r_n u - z_\eta v)(r_\xi u_\xi - z_\xi v_\xi) = (z_\xi^2 + r_\xi^2)P_\eta - (z_\xi z_\eta + r_\xi r_\eta)P_\eta, \tag{11}$$

where ξ and η represent the body-fitted coordinate lines, ξ being tangent to while η being normal to the solid wall. In the inlet/outlet planes, where flow conditions are specified, one-dimensional characteristic analysis based on Riemann invariants are used.

Figure 2 shows the grids and computation domain for the numerical study. Totally, there are 16,311 nodes and 16,000 cells. The number of cells is chosen based on the accuracy of computation and attainment of convergence. Regions I and III in Fig. 2 are the nozzle and free jet regions, respectively, each consisting of 5000 cells. Regions II and IV are in the vacuum chamber excluding the free jet region. Each cell is a polygon of four sides. Near the tip of the nozzle region and the boundary of the free jet region, the cells are more closely packed than the other regions for better accuracy. The tip of the nozzle is 750 μm in

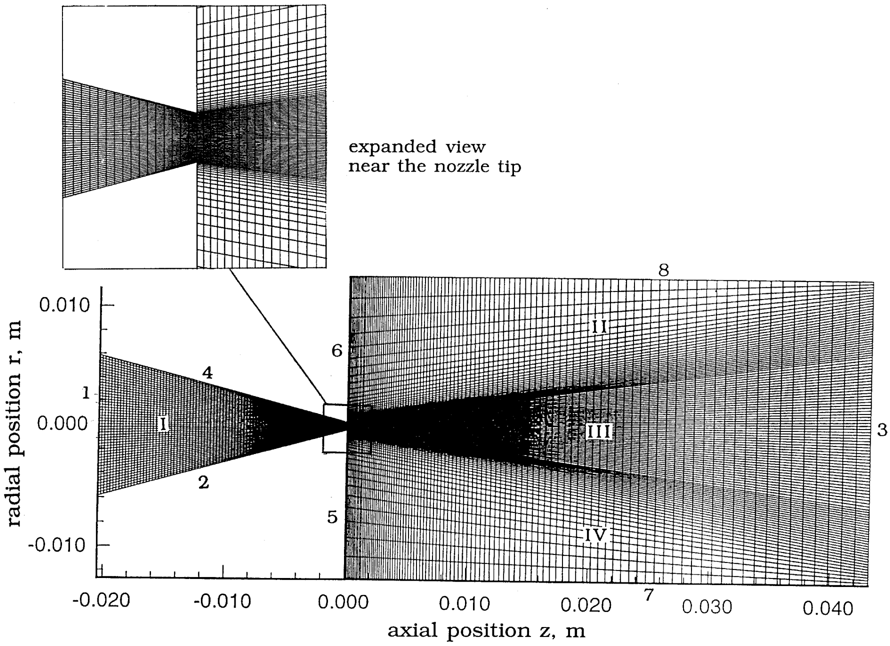

Fig. 2. Grids used in the computation domain. Boundary 1 on the left lies where the aerosol and sheath air flows enter the nozzle; $z = 0.0$ m corresponds to tip of the nozzle, $z = 0.001$ and 0.002 m correspond to the first and second laser beams.

diameter and the first and second laser beams are located 1 and 2 mm downstream of the nozzle, where the chamber pressure is 0.03 atm.

There are eight boundaries from 1 to 8 as shown in Fig. 2. Boundary 1 is the inlet of the nozzle where the sheath air and aerosol flow mixes. The values for flow velocity, ambient pressure and temperature are set at boundary 1. Boundaries 2, 4, 5 and 6 have zero vertical pressure gradient and zero vertical velocity component. Pressures at boundaries 3, 7 and 8 are set at 0.03 atm. In addition, the vertical pressure gradient at boundaries 7 and 8 are set to be zero.

According to the compressible flow theory, if the downstream pressure is less than 0.528 times the upstream pressure of the nozzle, the flow is choked. Under choked flow condition, it can be shown that the volumetric flow rate Q is independent of the ambient pressure but depends on ambient temperature T and nozzle diameter d_n as

$$Q = \frac{\pi}{4} d^2 \left(\frac{2}{\gamma + 1} \right)^{1/(\gamma - 1)} \sqrt{\frac{2\gamma R T}{\gamma + 1}}, \tag{12}$$

where R is the universal gas constant. The flow rate Q is calculated to be $5.3\,\mathrm{l\,min^{-1}}$ at $T = 20°\mathrm{C}$, which is very close to the measured value of $5.2\,\mathrm{l\,min^{-1}}$, as determined by a bubble flow meter, for the Aerosizer$^{\mathrm{TM}}$ in this study. The individual flow rates of sheath air and aerosol were measured separately and found to be 2.0 and $3.2\,\mathrm{l\,min^{-1}}$ respectively, which constituted the total flow rate of $5.2\ \mathrm{min^{-1}}$. The flow velocities are calculated to be 17 and $0.3\ \mathrm{m\,s^{-1}}$ for the aerosol and sheath air flow, respectively. These velocities were used as inputs at boundary 1.

Calculation of particle trajectory and τ_{TOF}

Particle trajectory and τ_{TOF} are calculated along the z-axis of the Aerosizer$^{\mathrm{TM}}$. The particle equation of motion can be written as

$$\frac{\mathrm{d}^2 z}{\mathrm{d}t^2} = C_d \frac{\mathrm{Re}}{24} \frac{(u - \mathrm{d}z/\mathrm{d}t)}{\tau}, \tag{13}$$

where τ is the particle relaxation time defined as $\tau = \rho_p d_p^2 C/18\mu$ (ρ_p, particle density; d_p, particle diameter; C, slip correction factor; μ, air dynamic viscosity). It was found that if equation (1) is used for calculating the drag coefficient C_d, the simulated particle τ_{TOF} would been much greater than the experimental data. Stated otherwise, the particles would be undersized.

The following expressions, which were originally developed by Henderson (1976) for a wide range of flow conditions taking into account the particle Mach number and particle Reynolds number, were therefore used in this study. In the subsonic flow regime, C_d is given as follows:

$$C_d = 24\left[\mathrm{Re}_p + S\left\{4.33 + \left(\frac{3.65 - 1.53\,T_w/T}{1 + 0.353T_w/T}\right)\exp\left(-0.247\frac{\mathrm{Re}_p}{S}\right)\right\}\right]^{-1}$$
$$+ \exp\left(-\frac{0.5M}{\sqrt{\mathrm{Re}_p}}\right)\left[\frac{4.5 + 0.38(0.03\mathrm{Re}_p + 0.48\sqrt{\mathrm{Re}_p})}{1 + 0.03\mathrm{Re}_p + 0.48\sqrt{\mathrm{Re}_p}} + 0.1M^2 + 0.2M^8\right]$$
$$+ \left[1 - \exp\left(-\frac{M}{\mathrm{Re}_p}\right)\right]0.6S. \tag{14}$$

In the supersonic regime at Mach numbers equal to or greater than 1.75, the expression for C_d is

$$C_d = \frac{0.9 + \dfrac{0.34}{M^2} + 1.86(M_\infty/\mathrm{Re}_\infty)^{1/2}\left[2 + \dfrac{2}{S_\infty^2} + \dfrac{1.058}{S_\infty}(T_w/T)^{1/2} - \dfrac{1}{S_{-}^4}\right]}{1 + 1.86(M_\infty/\mathrm{Re}_\infty)}. \tag{15}$$

In the supersonic regime at Mach number between 1.0 and 1.75, C_d is the linear interpolation of equations (14) and (15):

$$C_d(M_\infty, \mathrm{Re}_\infty) = C_d(1.0, \mathrm{Re}_p) + \tfrac{4}{3}(M_\infty - 1.0)[C_d(1.75, \mathrm{Re}_\infty) - C_d(1.0, \mathrm{Re}_p)], \tag{16}$$

where $C_d(1.0, \mathrm{Re}_p)$ is the value calculated using Equation (14) and $C_d(1.75, Re_\infty)$ represents the value calculated using Equation (15) with $M_\infty = 1.75$. In the above equations, M is the particle Mach number based on the relative velocity between the particle and air flow; S is the molecular speed ratio which is equal to $M\sqrt{\gamma/2}$, T_w is the temperature of the particle and T is the air temperature. Subscript ∞ in equations (15) and (16) denotes free stream conditions.

Figure 3 compares the magnitude of C_d calculated by Henderson's formula, (14)–(16), and those by the Rader and Marple formula (1b) and (1c), assuming the total flow rate of

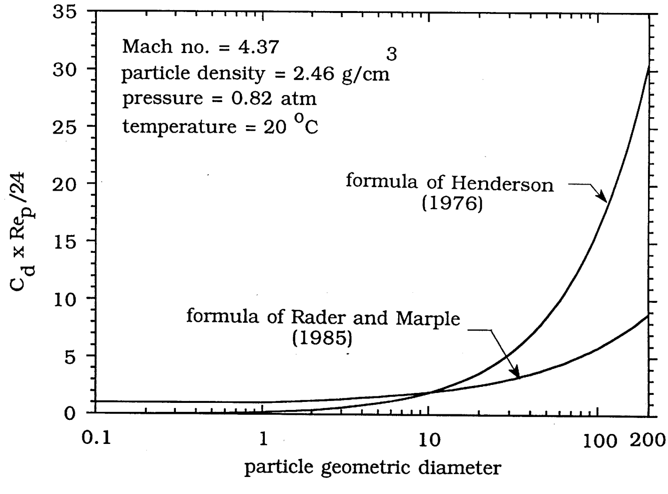

Fig. 3. Comparison of $C_d\mathrm{Re}_p/24$ as obtained by different formulae. Total volumetric flow rate is 5.2 l min^{-1}, ambient temperature and pressure are 20°C and 0.82 atm respectively.

$5.2\,\mathrm{l\,min^{-1}}$, ambient temperature of 20°C, ambient pressure of 0.82 atm and particle density of $2.46\,\mathrm{g\,cm^{-3}}$. The flow Mach number is 4.37 at the second laser beam of the Aerosizer™. It is seen that when the particle diameter is greater than about 10 μm, the effect of flow compressibility is to increase C_d over the value calculated by using the traditional incompressible flow formula. This increase in C_d becomes very substantial as the particle diameter becomes much greater than 10 μm. In this case, it is expected that particle τ_{TOF} will be much smaller when Henderson's formula is used to calculate C_d.

While Henderson's formula may be more accurate for supersonic flow, it predicts C_d values that are unreasonably low for small particles. For example, when particle diameter is less than 10 μm, the product of C_d and $\mathrm{Re_p}/24$ is less than 1.0, which is the lowest value that this term can take. In this case, equations (1) should be used instead.

EXPERIMENTAL

Monodisperse, spherical solid PSL, solid ammonium fluorescein and liquid oleic acid particles were generated in the laboratory to obtain the experimental data for particle τ_{TOF} versus particle diameters directly from the Aerosizer™. Liquid suspension containing PSL (Duke Scientific, Palo Alto, CA, U.S.A.) particles in the size range of 0.9–9.87 μm was generated by a Retec nebulizer (Cavitron Corp., U.S.A.). These particles were dried in a silica gel diffusion dryer and charge-neutralized by a TSI 3077 bi-polar electrostatic charge neutralizer before being introduced directly into the Aerosizer™ to obtain the particle τ_{TOF} data.

Solid ammonium fluorescein particles (size range, 2.89–25.6 μm) and liquid oleic acid particles (size range, 2.47–24.2 μm) were generated using an inverted Vibrating Orifice Monodisperse Aerosol Generator (VOMAG, TSI model 3450, St. Paul, MN, U.S.A.) (Vanderpool and Rubow, 1988; Tsai and Cheng, 1995). These particles were then dried and charge-neutralized. Similar to the PSL particles, these particles were introduced vertically into the Aerosizer™ located at the bottom to avoid particle transport loss. The experimental setup is shown in Fig. 4. Particle monodispersity was monitored by a TSI 33B Aerodynamic Particle Sizer. Liquid oleic acid particles were further collected using a fluorocarbon (3M FC-722) coated glass slide and observed under a microscope for obtaining the flattened diameter. The actual diameter was then calculated as a product of the observed flattened diameter and a flattening coefficient of 1.32 (Liu *et al.*, 1982). The flattening coefficient was, in turn, checked independently by comparing the observed

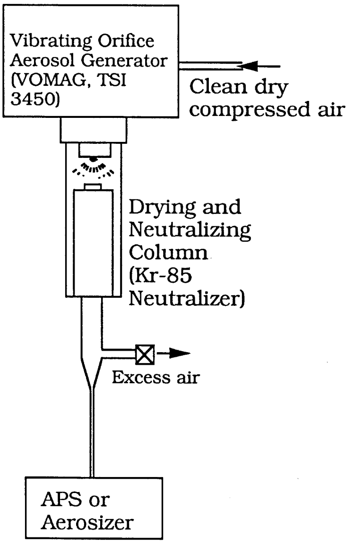

Fig. 4. Schematic diagram of the experimental setup.

diameter under a microscope and the true diameter as calculated theoretically from the operational parameters of the VOMAG (Berglund and Liu, 1973).

RESULTS AND DISCUSSION

Results of flow simulation

The flow field is plotted as constant velocity contours in Fig. 5a over the entire calculation domain, and in Fig. 5b, in the area of converging nozzle to show more detailed information. A still more detailed contour plot near the nozzle tip is shown in Fig. 6a. The ambient pressure and temperature are 1 atm and 20°C respectively. Similar flow fields were obtained when the ambient pressure was changed to 0.9, 0.8 or 0.7 atm. It can be seen from these figures that the air flow accelerates in the converging nozzle until it is choked at the tip of the nozzle when the Mach number becomes 1.0. Then the air flow expands from the tip of the nozzle into the low-pressure vacuum chamber. A Mach disk at about $z = 0.0029$ m is formed downstream of the second laser beam, $z = 0.002$ m.

Figure 5b shows that the aerosol flow velocity is much greater than that of sheath air near the nozzle inlet. The aerosol flow velocity remains high at about 17 m s^{-1} until z is near

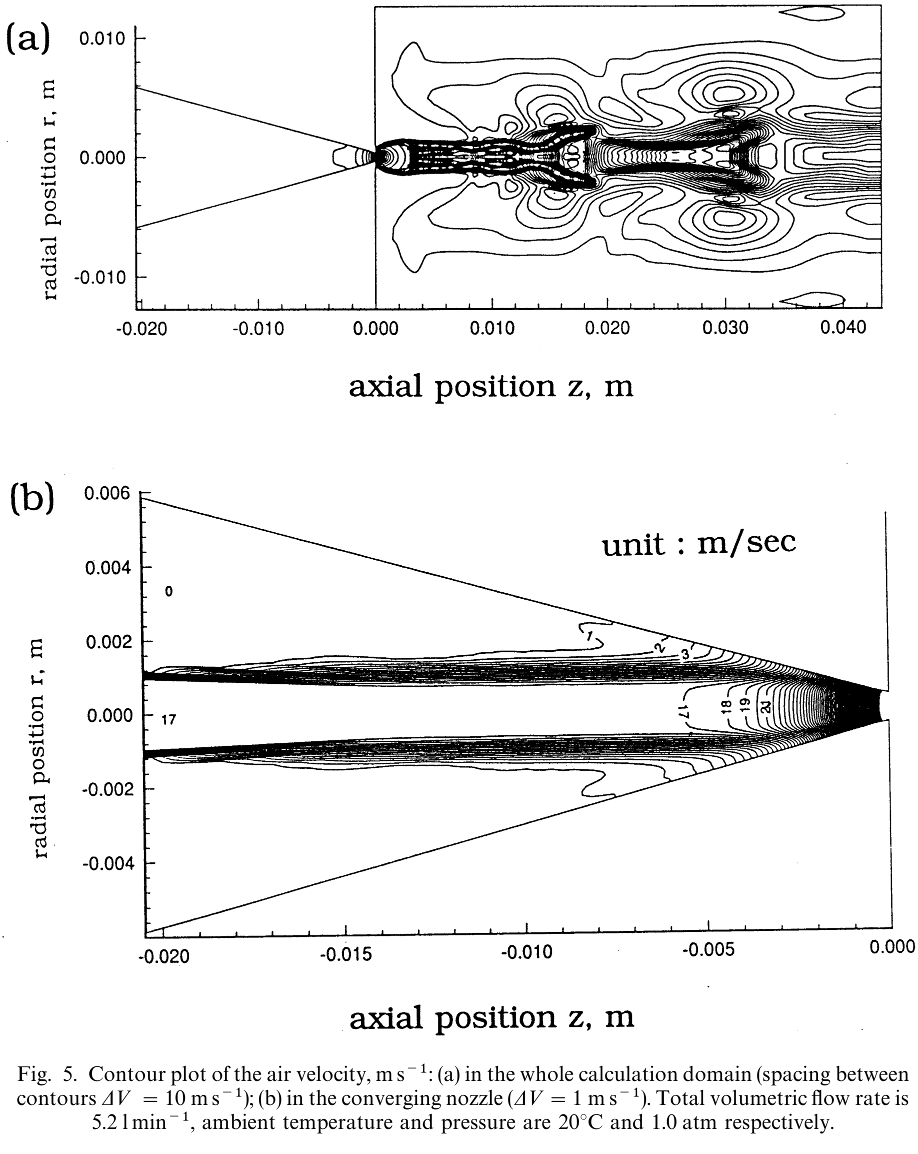

Fig. 5. Contour plot of the air velocity, m s^{-1}: (a) in the whole calculation domain (spacing between contours $\Delta V = 10$ m s^{-1}); (b) in the converging nozzle ($\Delta V = 1$ m s^{-1}). Total volumetric flow rate is 5.2 l min^{-1}, ambient temperature and pressure are 20°C and 1.0 atm respectively.

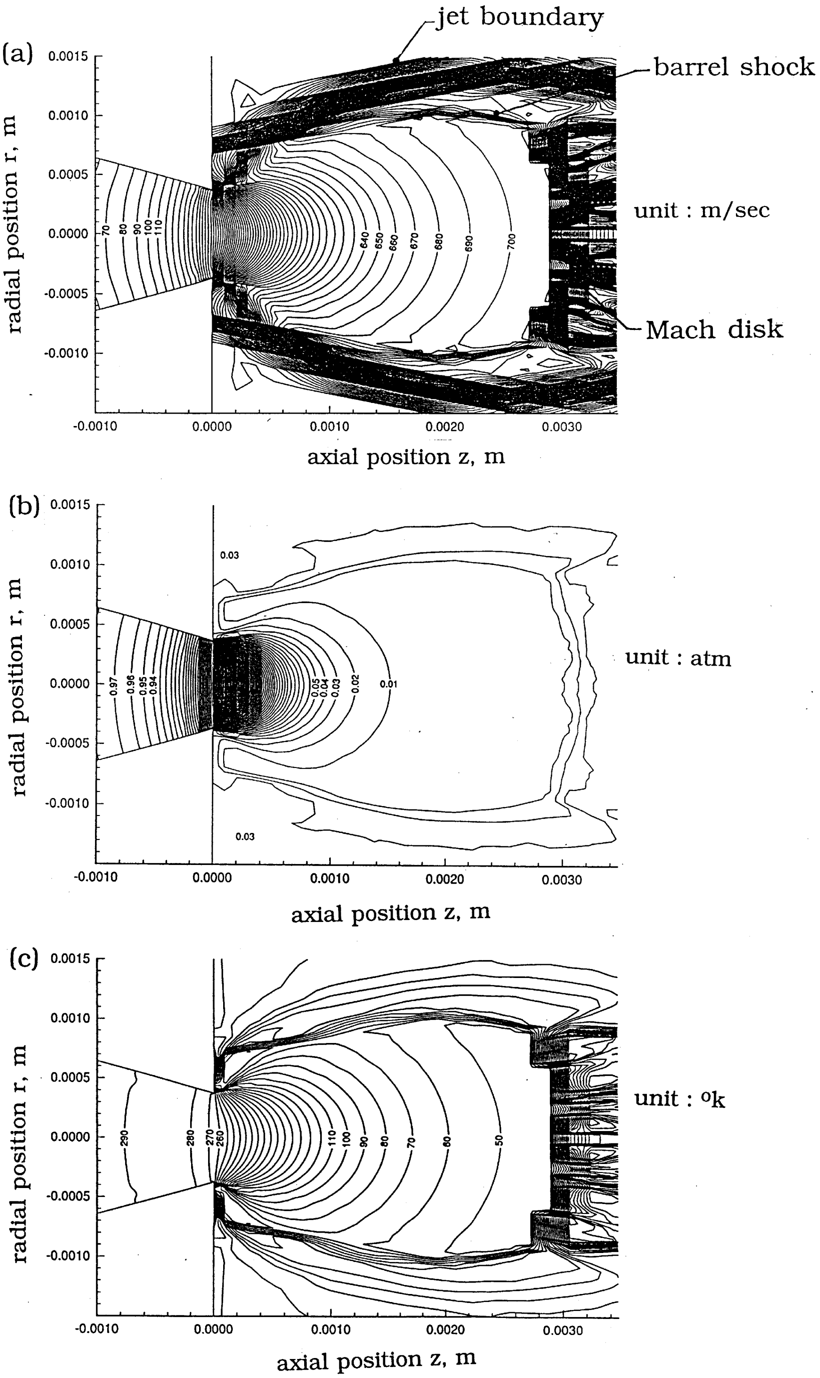

Fig. 6. Contour plot near the tip of the nozzle (a) air velocity, $\mathrm{m\,s^{-1}}$, (b) air pressure, atm, (c) air temperature, K. Total volumetric flow rate is $5.2\,\mathrm{l\,min^{-1}}$, ambient temperature and pressure are 20°C and 1.0 atm respectively.

– 0.005 m, when it starts to mix with the sheath air and accelerates to sonic speed. Obtaining this two-dimensional flow field becomes important for very large particles which may attain high enough velocities near the nozzle tip and, consequently, influence its τ_{TOF} across the two laser beams. As will be shown later, the prediction of particle τ_{TOF} is more accurate for large particles if this two-dimensional flow field is used for the τ_{TOF} calculation.

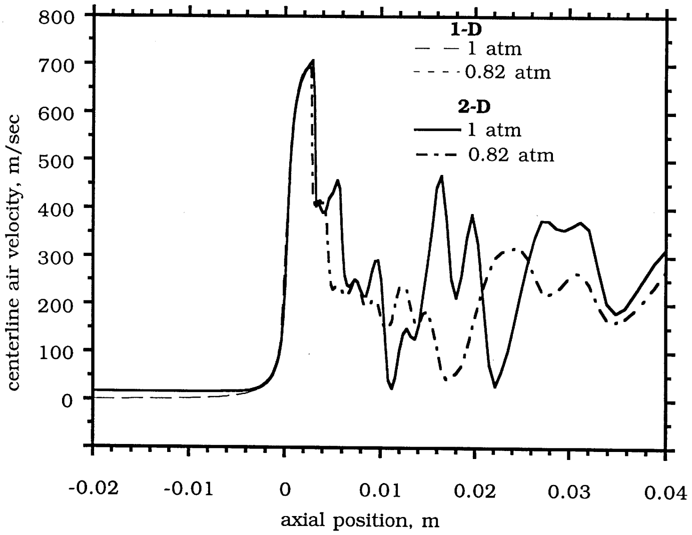

Fig. 7. Comparison of the centerline velocities, as calculated from different models. Total volumetric flow rate is $5.2\,\mathrm{l\,min^{-1}}$ and the ambient temperature is 20°C. (Note that the two curves of different pressure conditions for one- and two-dimensions, respectively, nearly overlap with each other before the Mach disk.)

More detailed contour plots of flow velocity, pressure and temperature near the nozzle tip are shown in Figs 6a–c. At the nozzle tip, the flow becomes sonic and there is a barrel shock at the downstream of the jet. The Mach disk appears more clearly at $z \approx 0.0029$ m where the centerline air flow velocity drops sharply. This is the case as the ambient pressure equals to 1.0 atm. Other calculations have shown that the location of the Mach disk, z, moves closer to the nozzle tip as the ambient pressure reduces below 1.0 atm, such that z equals to 0.0027, 0.0026 and 0.0024 corresponding to the ambient pressures of 0.9, 0.82 and 0.7 atm, respectively. It is anticipated that further reduction in the ambient pressure will move the location the Mach disc upstream of the second laser beam, which is clearly undesirable for the Aerosizer$^{\mathrm{TM}}$.

As the air jet expands from the nozzle tip, air pressure and temperature drop sharply to very low values. The lowest temperature and pressure occur near the front end of the Mach disc, which are 40 K and 0.01 atm, respectively.

Comparison of the centerline air velocities calculated from the two-dimensional flow (this study) and one-dimensional flow (Cheng et al., 1993) is shown in Fig. 7. It can be seen that the velocities are not very different for different ambient pressures as well as different flow assumptions. The major difference occurs within the converging nozzle where the one-dimensional flow assumption has to use an average velocity value for both aerosol and air flows. This results in underestimation of the centerline aerosol flow velocity which consequently overestimates the τ_{TOF} for large particles. More accurate particle τ_{TOF} is obtained by using the two-dimensional flow assumption, as will be shown later.

Comparison of theoretical and experimental τ_{TOF}

Comparison of the theoretical particle τ_{TOF} with the experimental data of Cheng *et al.* (1993) is presented in Fig. 8. The experimental data as well as the predictions were obtained at the reduced ambient pressure of 0.82 atm. It can be seen that for particles smaller than 10 μm in diameter, both original calibration and the present study predict particle τ_{TOF} accurately. However, the original calibration using one dimensional flow assumption and traditional formula for particle drag coefficient, equation (1), overestimates the experimental τ_{TOF} when the particle diameter is greater than 10 μm for both PSL and glass beads. The deviation from the original calibration becomes greater as the particle size increases. In contrast, the present

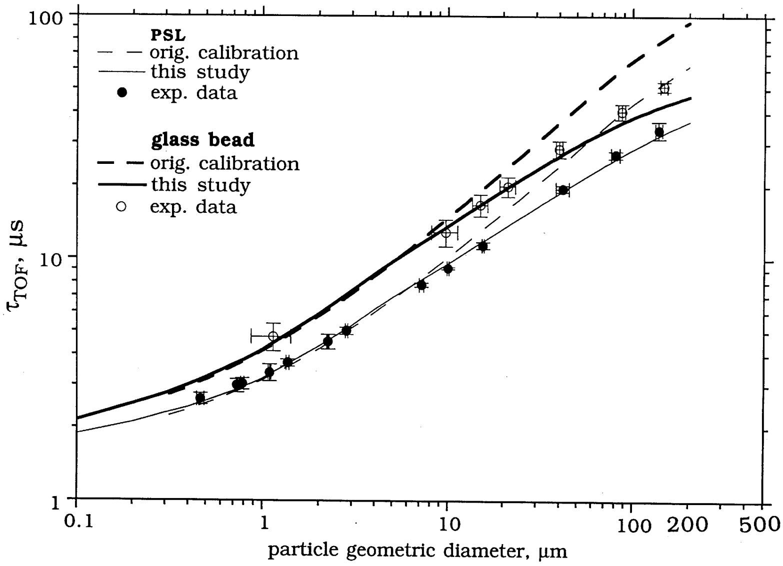

Fig. 8. Comparison of the theoretical τ_{TOF} with experimental data for PSL and glass beads (Cheng *et al.*, 1993), ambient pressure = 0.82 atm, temperature = 20°C.

study using two-dimensional flow assumption and correct particle drag coefficient, equations (14)–(16), predicts particle τ_{TOF} accurately for both PSL and glass beads, only except for the glass beads of 146 μm, for which the difference between experimental data and theoretical results is greater than 10%. The reason for this exceptional deviation is not clear yet.

To test whether the two-dimensional flow field predicts the particle τ_{TOF} more accurately than the one-dimensional flow field, a separate run using both flow fields and correct particle drag coefficient shows that one-dimensional flow assumption indeed still substantially overestimates τ_{TOF} for large particles. This means that, it is important to obtain an accurate air flow velocity data in the nozzle region to accurately predict the particle τ_{TOF}.

Comparison of the theoretical τ_{TOF} with experimental data obtained in this study for PSL and ammonium fluorescein particles is shown in Figs 9a and b, respectively. The ambient pressure and temperature are 1.0 atm and 20°C, respectively. It can be seen that within the size range (diameter of PSL $< 10\,\mu$m; diameter of ammonium fluorescein $< 26\,\mu$m) investigated, the current study is able to predict particle τ_{TOF} accurately for both PSL and ammonium fluorescein particles. The original calibration again overestimates particle τ_{TOF} when the particle diameter is greater than 10 μm.

Sizing accuracy of the Aerosizer™ for liquid oleic acid particles was also studied. The aerodynamic diameters as measured by the APS™ and Aerosizer™ were compared for this purpose with the actual aerodynamic diameters, as shown in Fig. 9c. The actual aerodynamic diameter was calculated from the operational parameters of the VOMAG. The aerodynamic diameter obtained from microscopic measurements and corrected by using the flattening coefficient is also indicated in the figure, which shows good agreement with the actual aerodynamic diameter. For the TSI APS™, the current experimental data are consistent with those of Baron (1986). Underestimation of the actual aerodynamic diameter is caused by particle deformation in the sensing zone of the instrument. It was found that the aerodynamic diameter measured by the Aerosizer™ is even smaller than that measured by the APS™. It is speculated that a greater deformation due to the higher air jet flow velocity must have occurred in the sensing zone of the Aerosizer™ than the APS™.

Effects of ambient pressure and particle density on τ_{TOF}

The effects of ambient pressure and particle density on particle τ_{TOF} were studied. Figure 10 compares the particle τ_{TOF}s versus a modified Stokes' number, St, similar to that

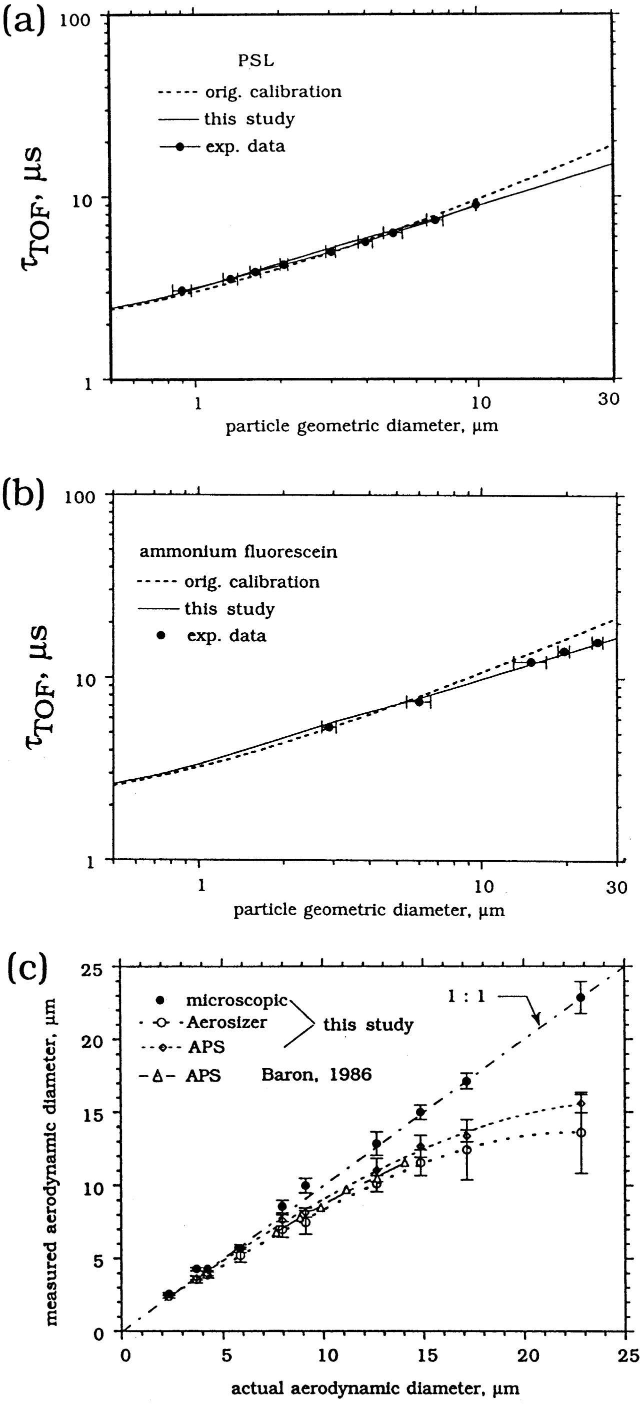

Fig. 9. Comparison of the theoretical τ_{TOF} with present experimental data, ambient pressure = 1 atm, temperature = 20°C: (a) PSL, (b) ammonium fluorescein, (c) oleic acid.

of Cheng *et al.* (1993) for different densities under different ambient pressures. The ambient temperature is assumed to be 20°C. The modified St is defined as

$$\mathrm{St} = \frac{\tau c_g}{D(1 + \frac{1}{6}\mathrm{Re}_p^{2/3})}, \tag{17}$$

where D is the nozzle diameter and c_g is the air velocity at the nozzle exit. The flow conditions at the nozzle exit were used to calculate the particle relaxation time τ and

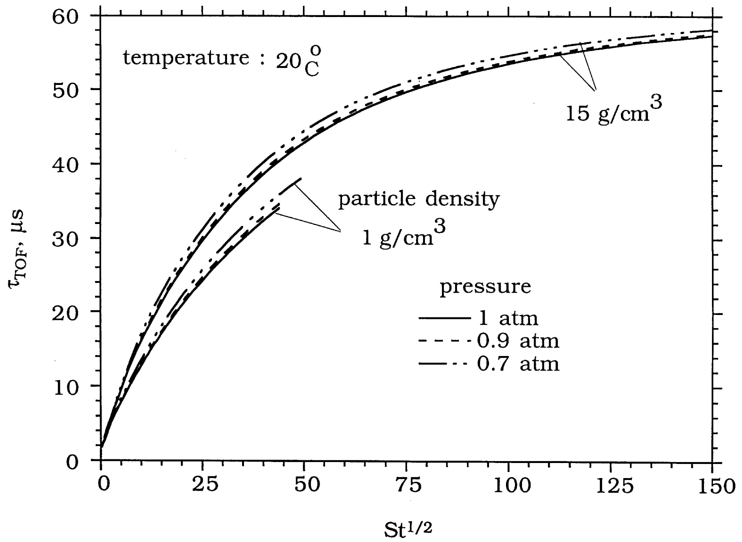

Fig. 10. Comparison of particle τ_{TOF} for particles with different densities under different ambient pressures, ambient temperature = 20°C.

particle Reynolds number Re_p. It can be seen from the figure that both particle density and inlet pressure have an effect on particle τ_{TOF}. Lower ambient pressure and greater particle density result in higher particle τ_{TOF}. However, the effect of ambient pressure, in the range 0.7–1.0 atm, is not very significant if particle density is fixed. Nevertheless, there is no single one-to-one correlation between the particle τ_{TOF} and the modified St, as shown in Cheng *et al.* (1993). It is suspected that, in the study by Cheng *et al.* (1993), the range of particle densities was not large enough to discern the differences that may exist. In this study, an attempt to use another form of the modified St, based on the correct particle drag formula, i.e. equations (14)–(16), to correlate particle τ_{TOF} was not successful.

CONCLUSIONS

This paper has studied the performance of an API Aerosizer^{TM} numerically as well as experimentally. In the previous studies on the API Aerosizer^{TM}, there has been a lack of agreement between the experimental particle τ_{TOF} and theoretical predictions. The previous theoretical predictions were based on the one-dimensional flow field in the nozzle region and the particle equation of motion which used drag coefficient applicable for incompressible flow regime only. In the present study, a numerical method has been developed to obtain more accurate and detailed two-dimensional supersonic flow field and particle trajectory in the API Aerosizer^{TM}.

The theoretical particle τ_{TOF} results from the present experimental data were compared with those of Cheng *et al.* (1993). Good agreement was found for solid particles. For particles larger than 10 μm in diameter, the original τ_{TOF} calibration curve for the API Aerosizer^{TM} was found to overestimate the experimental data mainly because of incorrect use of the particle drag coefficient in the supersonic flow field and the assumption of one-dimensional flow field in the nozzle region. For large particles, significant effects of ambient conditions and particle density on particle τ_{TOF} were found. However, a single modified St which produces a one-to-one relationship between particle τ_{TOF} and St, regardless of the ambient conditions and particle densities has not yet been found.

Aerodynamic diameter of liquid particles were found to be underestimated more by the API Aerosizer^{TM} than the TSI APS^{TM}. It is speculated that a larger deformation of the liquid particles occurred in the API Aerosizer^{TM} than that in the TSI APS^{TM} because of higher air flow velocity in the former. Further study using liquid particles larger than 25 μm is necessary to confirm this speculation.

In addition to the problems related to the sizing accuracy of the Aerosizer$^{\text{TM}}$, its counting accuracy also deserves attention. Recently, Baron *et al.* (1996) found that the Aerosizer$^{\text{TM}}$ has low inlet efficiency and low counting efficiency for oil droplets when compared to simultaneous APS$^{\text{TM}}$ measurements. It is important for aerosol researchers to explore the cause of these problems further. In the future, counting efficiency and its dependence on particle aerodynamic diameter will be investigated using the detailed two dimensional flow field obtained in this study.

Acknowledgement— Authors would like to thank the Ministry of Economic Affairs, Republic of China, for the financial support under grant No. 85-EC-2-A-17-0111 during the 1995–1996 fiscal year.

REFERENCES

Ananth, G. and Wilson, J. C. (1988) Theoretical analysis of the performance of the TSI aerodynamic particle sizer. *Aerosol Sci. Technol.* **9,** 189–199.

Anderson, W. K., Thomas, J. L. and van Leer, B. (1986) Comparison of finite volume flux vector splittings for the Euler equations. *AIAA J.* **24,** 1453–1460.

Ashkenas, H. and Sherman, F. (1966) *Rarefied Gas Dynamics* (Edited by de Leeuw, J. H.). Academic Press, New York.

Baron, P. A. (1986) Calibration and use of the aerodynamic particle sizer (APS 3300). *Aerosol Sci. Technol.* **5,** 55–67.

Baron, P. A., Mazumder, M. K. and Cheng, Y. S. (1993) Direct-reading techniques using optical particle detection. In *Aerosol Measurement* (Edited by Willeke and Baron), Chap. 17, pp. 381–409. Van Nostrand Reinhold, New York.

Baron, P. A., Yacher, J. M. and Heitbrink, W. A. (1996) Some observations on the response of the aerosizer to oil droplets in the 4–18 micrometer range. *Paper presented at the 15th Annual Conf.* 14–18 October, Orlando, FL.

Brockmann, J. E. and Rader, D. J. (1990) APS response to nonspherical particles and experimental determination of dynamic shape factor. *Aerosol Sci. Technol.* **13,** 162–172.

Berglund, R. N. and Liu, B. Y. H. (1973) Generation of monodisperse aerosol standards. *Envir. Sci. Technol.* **7,** 147–153.

Chen, B. T., Cheng, Y. S. and Yeh, H. C. (1985) Performance of a TSI aerodynamic particle sizer. *Aerosol Sci. Technol.* **4,** 89–97.

Chen, B. T., Cheng, Y. S. and Yeh, H. C. (1990) A study of density effect and droplet deformation in the TSI aerodynamic particle sizer. *Aerosol Sci. Technol.* **12,** 278–285.

Cheng, Y. S., Barr, E. B., Marshall, I. A. and Mitchell, J. P. (1993) Calibration and performance of an API Aerosizer. *J. Aerosol Sci.* **24,** 501–514.

Cheng, Y. S., Chen, B. T. and Yeh, H. C. (1990) Behavior of isometric nonspherical aerosol particles in the aerodynamic particle sizer. *Aerosol Sci. Technol.* **21,** 701–710.

Cheng, Y. S. and Dahneke, B. E. (1979) Properties of continuum source particle beams. II. Beams generated in capillary expansions. *J. Aerosol Sci.* **10,** 363–368.

Dahneke, B. (1973) Aerosol beam spectrometry. *Nature Phys. Sci.* **244,** 54–55.

Dahneke, B. E. and Cheng, Y. S. (1979) Properties of continuum source particle beams. I. Calculation methods and results. *J. Aerosol Sci.* **10,** 257–274.

Dahneke, B. E. and Padliya, D. (1977) Nozzle-inlet design for aerosol beam. In *Rarefied Gas Dynamics* (Edited by Potter, J. L.), Vol. 51, Part II, pp. 1163–1172, A.I.A.A., New York.

Griffiths, W. D., Iles, P. J. and Vaughan, N. P. (1986) The behaviour of liquid droplet aerosols in an APS 3300. *J. Aerosol Sci.* **17,** 921–930.

Heitbrink, W. A., Baron, P. A. and Willeke, K. (1991) Coincidence in time-of-flight spectrometers: Phantom particle creation. *Aerosol Sci. Technol.* **14,** 112–126.

Henderson, C. B. (1976) Drag coefficients of spheres in continuum and rarefied flows. *AIAA J.* **14,** 707–708.

Kinney, P. D. and Pui, D. Y. H. (1995) Inlet efficiency study for the TSI aerodynamic particle sizer. *Part. Part. Syst. Charact.* **12,** 188–193.

Lee, K. W., Kim, J. C. and Han, D. S. (1990) Effects of gas density and viscosity on response of aerodynamic particle sizer. *Aerosol Sci. Technol.* **13,** 203–212.

Liu, B. Y. H., Pui, D. Y. H. and Wang, X. Q. (1982) Drop size measurement of liquid aerosols. *Atmos. Envir.* **16,** 563–567.

Marshall, I. A., Mitchell, J. P. and Griffiths, W. D. (1991) The behaviour of regular-shaped non-spherical particles in a TSI aerodynamic particle sizer. *J. Aerosol Sci.* **22,** 73–89.

Rader, D. J., Brockmann, J. E., Ceman, D. L. and Lucero, D. A. (1990) A method to employ the APS factory calibration under different operating conditions. *Aerosol Sci. Technol.* **13,** 514–521.

Rader, D. J. and Marple, V. A. (1985) Effect of ultra-Stokesian drag and particle interception on impaction characteristics. *Aerosol Sci. Technol.* **4,** 141–156.

Roe, P. L. (1981) Approximate Riemann solvers, parameter vectors, and difference schemes. *J. Comput. Phys.* **43,** 357–372.

Tsai, C. J. and Cheng, Y. H. (1995) Solid particle collection characteristics on impaction surfaces of different designs. *Aerosol Sci. Technol.* **23,** 96–106.

Wang, H. C. and John, W. (1987) Particle density correction for the aerodynamic particle sizer. *Aerosol Sci. Technol.* **6,** 191–198.

Wang, H. C. and John, W. (1989) A simple iteration procedure to correct for the density effect in the aerodynamic particle sizer. *Aerosol Sci. Technol.* **10,** 501–505.

Whitaker, D. L., Grossman, B. and Lohner, R. (1989) Two-dimensional Euler computations on a triangular mesh using an upwind, finite-volume scheme. AIAA Paper 89-0470.

Vanderpool, R. W. and Rubow, K. L. (1988) Generation of large, solid, monodisperse calibration aerosols. *Aerosol Sci. Technol.* **9,** 65–69.